An analysis of the acoustic cavitation noise spectrum: The role of periodic shock waves

Jae Hee Song, Kristoffer Johansen, and Paul Prentice[a)]
Cavitation Laboratory, School of Engineering, University of Glasgow, Glasgow G12 8QQ, United Kingdom

(Received 14 June 2016; revised 17 August 2016; accepted 15 September 2016; published online 12 October 2016)

Research on applications of acoustic cavitation is often reported in terms of the features within the spectrum of the emissions gathered during cavitation occurrence. There is, however, limited understanding as to the contribution of specific bubble activity to spectral features, beyond a binary interpretation of stable versus inertial cavitation. In this work, laser-nucleation is used to initiate cavitation within a few millimeters of the tip of a needle hydrophone, calibrated for magnitude and phase from 125 kHz to 20 MHz. The bubble activity, acoustically driven at $f_0 = 692$ kHz, is resolved with high-speed shadowgraphic imaging at 5×10^6 frames per second. A synthetic spectrum is constructed from component signals based on the hydrophone data, deconvolved within the calibration bandwidth, in the time domain. Cross correlation coefficients between the experimental and synthetic spectra of 0.97 for the $f_0/2$ and $f_0/3$ regimes indicate that periodic shock waves and scattered driving field predominantly account for all spectral features, including the sub-harmonics and their over-harmonics, and harmonics of f_0.

[http://dx.doi.org/10.1121/1.4964633]

[MFH] Pages: 2494–2505

I. INTRODUCTION

The acoustic cavitation spectrum offers a convenient and concise method for presenting cavitation data, summarizing the frequency content of the signal collected from a cavitating system, during an acoustic exposure. A typical cavitation spectrum, associated with acoustic driving of intermediate or high intensity, at a fundamental driving frequency of f_0, is rich in spectral features including peaks at nf_0, and at sub-multiple values, nf_0/m, known as the sub-harmonics, and the respective over-harmonics, at values greater than f_0. The sub-harmonics, and higher-order sub-harmonics, for $m > 2$, are generally held to be exclusive to the occurrence of cavitation activity within the medium hosting the acoustic exposure,[1] and are often reported as occurring simultaneously to their over-harmonics. Over-harmonics of the fundamental at nf_0 can form due to non-linear propagation.[2] However, as the presence of bubbles within the medium will be highly scattering, cavitation activity may be expected to make significant contributions at these frequency values, too.

In many studies seeking to develop industrial and medical applications of cavitation, features within the spectrum are linked or correlated to the cavitation effect under consideration. For example, Schoellhammer *et al.*,[3] recently demonstrated cavitation mediated drug delivery across the gastrointestinal wall, driven by a trans-rectal 20 kHz acoustic probe. Emissions at $f_0/2$ and $2f_0$ were used to monitor for bubble activity during exposure, and it was concluded that transient cavitation was predominantly responsible for molecular transportation. In another study that demonstrated microbubble-mediated blood-brain barrier disruption, with focused ultrasound at 550 kHz under MR-guidance, O'Reilly and Hynynen[4] monitored $3f_0/2$ and $5f_0/2$ in real time, as part of an active control feedback loop to the acoustic source. In yet another report employing many detection modalities to monitor cavitation and boiling in *ex vivo* tissue, exposed to high-intensity focused ultrasound (HIFU) at 1.69 MHz, McLaughlan *et al.*[5] used $4f_0$ following a high-pass filtering protocol. The authors noted some contribution from non-linear propagation, and that $4f_0$ had good temporal coincidence with broadband emissions and was sensitive to the occurrence of boiling.

However, verified accounts of the bubble-based origin of the cavitation emission signal, and particularly the contribution to the various features within a cavitation spectrum, are not common. The sub-harmonics, higher-order sub-harmonics and the respective over-harmonics have, in particular, eluded explanation, since they were first identified by Esche.[6] Suggested mechanisms include the establishment of surface waves along the bubble wall[7] and sub-harmonic oscillations from larger bubbles within a population,[8] with each receiving little experimental corroboration. One obvious consequence of this deficit is an inability to correlate a cavitation-mediated effect with actual bubble behavior, although it is generally recognized that the collapsing bubbles, and bubble structures, play a key role in many applications,[9,10] and that acoustic emissions are coupled to bubble dynamics.[11,12]

We recently reported periodic shock waves (PSWs), from cavitation clouds collapsing sub-harmonically in response to HIFU driving, as a source of the sub-harmonic signal.[13] In the current paper, we develop a simple spectral analysis model to assess the spectral contributions made by PSWs. The model is verified via acoustic detection of

[a)]Electronic mail: paul.prentice@glasgow.ac.uk

cavitation activity, resolved by high-speed shadowgraphic imaging, in close proximity to the tip of a PVdF needle hydrophone calibrated for phase and magnitude from 125 kHz to 20 MHz. A synthetic signal is constructed, based on components identified within the experimentally measured and hydrophone deconvolved emissions, allowing quantitative analysis of the relative contributions to the spectrum.

II. METHODS

A. Theory

1. Spectral analysis model for periodic shock waves

To assess the role of PSWs on the cavitation spectrum a simple generic model is developed. Five PSWs are considered, $x_{\mathrm{PSW}}(t)$, Fig. 1(a), in an idealized case for which the period of emission, T_{PSW}, and the peak-positive pressure amplitude, $\mathrm{PPPA}_{\mathrm{SW}}$, of each component shock wave is constant.

An impulse train, $c_T(t)$, is multiplied and convolved with a rectangular window function, $w_D(t)$, where D represents the duration of the shock wave train and $s(t)$, a shock wave function, Fig. 1(b),

$$x_{\mathrm{PSW}}(t) = c_T(t) \times w_D(t) * s(t), \tag{1}$$

such that $c_T(t) = \sum_{k=-\infty}^{\infty} \delta(t - k/T_{\mathrm{PSW}})$, $(k \in \mathbb{N})$, where δ is the Dirac delta function and $w_D(t) = \Pi(t/D)$.

The Fourier transform (FT) of Eq. (1), $X_{\mathrm{PSW}}(f)$, can be represented as

$$X_{\mathrm{PSW}}(f) = C_T(f) * W_D(f) \times S(f), \tag{2}$$

such that $C_T(f) = 1/T_{\mathrm{PSW}} \sum_{k=-\infty}^{\infty} \delta(t - 2\pi f_{\mathrm{PSW}} k)$, where $f_{\mathrm{PSW}} = 1/T_{\mathrm{PSW}}$, and $S(f)$ is the spectrum of a single shock wave, and $W_D(f) = D\,\mathrm{sinc}(fD)$.

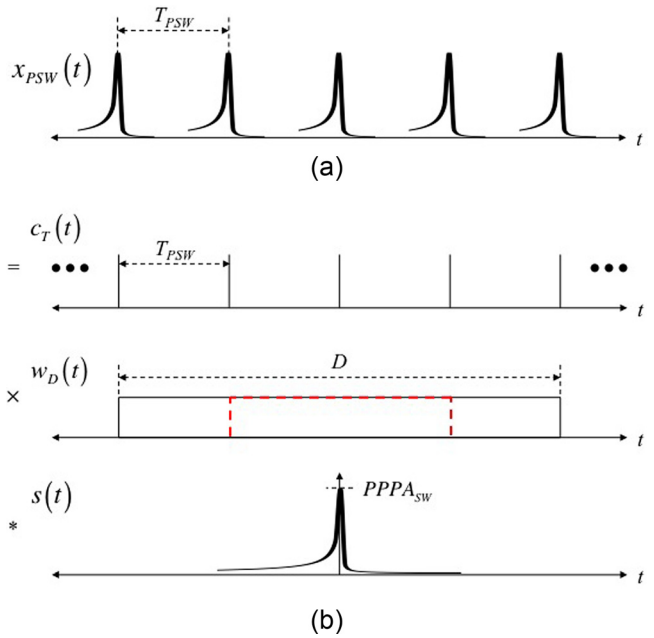

FIG. 1. (Color online) Representation of the spectral analysis model for periodic shock waves, in the time domain.

Figure 2(a), the spectrum of Fig. 1(a), indicates that PSWs are manifested as a series of peaks at nf_{PSW}, $C_T(f)$, the FT of $c_T(t)$ is itself an impulse train. The width of each spectral peak is determined by $W_D(f)$, the FT of $w_D(t)$. The magnitude of the spectral peaks decrease at the same rate as the spectral content of the shock wave, $S(f)$ [see Fig. 2(b)]. The spectral peaks for the three shock wave representation are wider, compared to those for five, due to the shorter duration of the window function [see Fig. 1(b)].

Therefore, for a cavitation cloud driven by ultrasound at a fundamental frequency f_0, in a regime where strong cloud collapses and shock wave emission occur at the half-harmonic, such that $f_{\mathrm{PSW}} = f_0/2$, PSWs may be expected to contribute to all spectral features at $nf_0/2$, including nf_0.

As demonstrated by Johnston *et al.*,[13] increasing the pressure amplitude of the acoustic driving generates cloud collapses that occur at higher-order sub-multiples, nf_0/m, for $m > 2$. For such regimes, PSWs may be expected to contribute to all features at nf_0/m.

2. The bubble collapse shock wave

It is known that the shock wave emitted by a collapsing bubble is quite distinct from other underwater shock waves, such as generated for lithotripsy,[14] or when a laser pulse is focused into a liquid, to generate a laser-induced bubble[15] [see Fig. 12(a) in the Appendix]. In the latter case, the optical breakdown shockwave (OBSW) is characterized by a sharp rise, from ambient pressure to the $\mathrm{PPPA}_{\mathrm{SW}}$ within the profile, of a few ns or less. In contrast, the bubble collapse shock wave (BCSW) has a smoother transition, or more gradual rise, as the non-linearity of the bubble wall motion gradually increases through the deflation and into the collapse[16] [see Fig. 12(b) in the Appendix]. The use of a generic shock wave function, such as the Church equation[17] would therefore be inappropriate in terms of adapting the spectral analysis model outlined above, to PSWs emitted from an acoustically driven bubble, or bubble cloud.

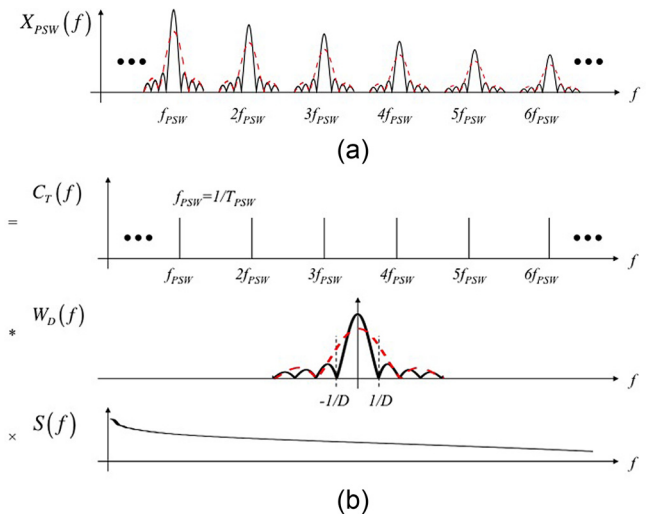

FIG. 2. (Color online) Representation of the spectral analysis model for periodic shock waves, in the frequency domain, for three shock waves (red dash), and five shock waves (solid black).

To simulate a BCSW profile for $s(t)$, the Gilmore equation for bubble oscillations is solved for a freely collapsing bubble in water. As the Gilmore equation depends on the liquid enthalpy, H, at the bubble wall, it is reasonably suited to studying inertial collapses.[18] In this work, the formulation presented by Kreider *et al.*[19] is used with some modifications, with the Gilmore equation given by

$$\left(1-\frac{\dot{R}}{C}\right)R\ddot{R}+\frac{3}{2}\left(1-\frac{\dot{R}}{3C}\right)\dot{R}^2 = \left(1+\frac{\dot{R}}{C}\right)H+\left(1-\frac{\dot{R}}{C}\right)\frac{R}{C}\dot{H}, \tag{3}$$

where the overdot represents the time derivative, R is the instantaneous radius, and C the instantaneous speed of sound evaluated at the bubble wall. H and C are given by

$$H=\frac{(b\Gamma)^{-1/\Gamma}}{\rho_0}\frac{\Gamma}{\Gamma-1}\left[(p_w-B)^{(\Gamma-1)/\Gamma}-(p_0+B)^{(\Gamma-1)/\Gamma}\right], \tag{4}$$

$$C^2=c_0^2+(\Gamma-1)H, \tag{5}$$

where ρ_0 is the ambient density of the surrounding liquid, c_0 the ambient speed of sound in the surrounding liquid, Γ is an empirically determined constant,[20] with b and B defined as $b=(\rho_0 c_0^2)^{-1}$ and $B\equiv(b\Gamma-p_0)^{-1}$, respectively. The pressure outside the bubble wall, p_w, is given by

$$p_w=p_i-\frac{4\mu\dot{R}}{R}-\frac{2\sigma}{R}, \tag{6}$$

where p_i is the internal pressure in the bubble, μ is the shear viscosity of the surrounding liquid and σ the surface tension at the gas-liquid interface. Assuming that the internal pressure is uniform, it can be represented as

$$p_i=\left(p_0+\frac{2\sigma}{R_0}\right)\left(\frac{R_0}{R}\right)^{3\kappa}, \tag{7}$$

where R_0 is the equilibrium radius of the bubble, and κ is the polytropic exponent. The high-speed observations of Fig. 6(c), described below, indicate that a single bubble has a maximum radius $R_{\max}\sim 50\,\mu$m. The equilibrium radius, $R_0=4.4\,\mu$m, was estimated from the Minnaert equation,[21] based on the experimental driving frequency, $f_0=692$ kHz.

Equation (3) was solved using the ode45 algorithm of MATLAB (MathWorks Inc., Natick, MA) with the following parameters: $c_0=1484\,\mathrm{ms}^{-1}$, $p_0=101\,\mathrm{kPa}$, $\Gamma=6.5$, $\kappa=4/3$, $\rho_0=998\,\mathrm{kgm}^{-3}$, $\sigma=0.072\,\mathrm{Nm}^{-1}$ and $\mu=0.001$ Pa s.

From the numerical solution of Eq. (3), the acoustic emission can be calculated as a spherical wave, P_{rad}, in the following way:[22]

$$P_{\mathrm{rad}}=\rho_0\frac{R^2\ddot{R}+2R\dot{R}^2}{r}, \tag{8}$$

where r is distance from the center of the cavity. We note that Eq. (8) assumes linear propagation. Figure 3 shows the simulation of a freely collapsing bubble, and its shock wave emission, as predicted by Eq. (8), at a distance of 3 mm from the center of the cavity. The simulated shock wave profile represented in Fig. 3, is denoted $s_{\mathrm{sim}}(t)$, and forms the basis of the synthetic spectra construction, described below.

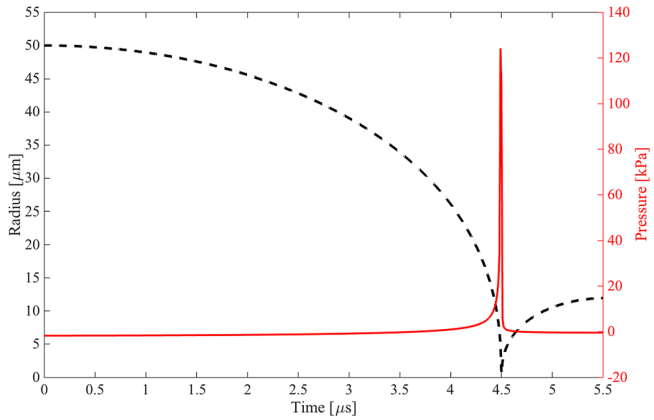

FIG. 3. (Color online) Simulated radius-time curve (black dash) and bubble collapse shock wave (solid red) for a free bubble of equilibrium and maximum radii, $R_0=4.4\,\mu$m and $R_{\max}=50\,\mu$m, respectively.

B. Experiment

1. The experimental set-up

The experimental arrangement depicted in Fig. 4(a) is used to study cavitation in unprecedented detail, both optically and acoustically. HIFU is generated via a single element piezoceramic transducer (H-149, Sonic Concepts, Bothell, WA), connected to a power amplifier (2100L, Electronic and Innovation, Rochester, NY) and a waveform generator (DG4102, Rigol Technologies, Beijing, China). The transducer has an outer diameter of 110 mm and is geometrically focused to 68 mm from the front face. The HIFU transducer has a natural fundamental frequency at 200 kHz, however, for the current work it is driven at the third harmonic through an impedance matching network, such that $f_0=692$ kHz for all results presented. This driving frequency is chosen so that acoustic cavitation emissions are well within the calibration bandwidth of the needle hydrophone (NH, 1.0 mm diameter, PVdF, Precision Acoustics, Dorchester, UK) discussed Sec. II B 3. A 20 mm central hole, through the body of the transducer, serves to mount the NH, aligned vertically along the HIFU axis, Fig. 4(a), with the tip located around the pre-focus −6 dB contour, ∼3 mm from the focal point. We refer to this orientation as the "emission collection" position, Fig. 4(b). The NH is connected to an oscilloscope (MS07104A, Agilent Technologies, Lexington, MA), and data collected at 4 GSs^{-1}. We recognize that, in this location, the presence of the NH will cause some perturbation to the field, which we have taken a number of steps to assess in Sec. II B 2.

To precisely initiate cavitation activity relative to the NH tip, and in the HIFU focus, we employ the laser-nucleation technique.[23] A single 1.2 ± 0.1 mJ (instrument error according to manufacturer), 6–8 ns laser pulse (Nano S 130-10 frequency doubled Q-switched Nd:YAG, Litron

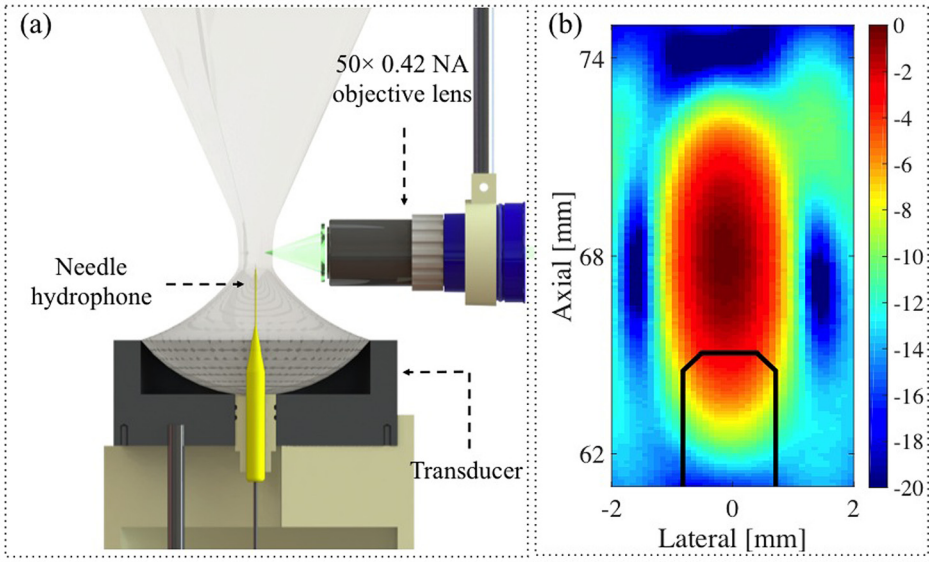

FIG. 4. (Color online) Illustration of experimental setup: (a) cross-sectional side view, and (b) an axial scan of the HIFU focal region, with representations of the NH outlined for "emission collection" position (solid black).

Lasers, Rugby, UK), is passed through a long working distance microscope objective lens (50×0.42 NA Mitutoyo, Kawasaki, Japan), submerged in a sealed unit, mounted on an xyz manipulator (Velmex Motor, Bloomfield, NY), and pre-aligned to the HIFU focus, ~3 mm above the NH tip *in situ*. The laser pulse, triggered to be incident ~5 cycles into a 65-cycle burst of HIFU, generated the cavitation activity reported below.

The transducer-NH configuration is housed within a custom-built chamber, measuring $420 \times 438 \times 220\,\text{mm}^3$ and filled with degassed, deionized water. Two of the walls of the chamber are recessed, to allow the placement of imaging optics in proximity to the intended location of the cavitation, facilitating reasonably high spatial resolution imaging.

High-speed shadowgraphic imaging of the resulting cavitation activity is undertaken orthogonally to the nucleating laser axis, through a Monozoom 7 lens system (Bausch & Lomb, Rochester, NY), at 5×10^6 frames per second (HPV-X2, Shimadzu, Kyoto, Japan), with synchronous 10 ns laser pulses (CAVILUX Smart, Cavitar, Tampere, Finland) providing the illumination and effective temporal resolution, per frame. A delay generator (DG535, Stanford Research Systems, Sunnyvale, CA) provides electronic triggering to synchronize each of the instruments. The Q-switch of laser, which is detected by the NH (see Fig. 12 in the Appendix), signifies laser pulse emission and cavitation nucleation, and is taken as $t = 0$ μs.

2. Assessment of HIFU field perturbation

To assess the effect of placing the NH in the emission collection position a fiber-optic hydrophone (FOH, Precision Acoustics) is introduced with the tip aligned to the HIFU focus, Figs. 5(a) and 5(b), and the point to which the cavitation nucleating laser pulse is focused. The FOH sensitivity below 1 MHz is quite unstable, however with a tip size of 125 μm and a fiber diameter of 10 μm (the effective active area), it does have the advantage of sampling the specific region of the field at which cavitation will be introduced. The FOH is calibrated for 692 kHz, via the substitution method with the NH placed in an equivalent position, across a range of $\text{PPPA}_{\text{HIFU}}$'s.

Two $\text{PPPA}_{\text{HIFU}}$ values were used to drive cavitation, for the results presented below as $f_0/2$ and $f_0/3$ regimes. The FOH measurements in free-field conditions (validated with the NH) indicated $\text{PPPA}_{\text{HIFU}} = 1.94 \pm 0.13$ and 2.84 ± 0.15 MPa (average $\pm$ standard deviation, over at least 20 measurements), respectively, for each of these regimes. With the NH in the emission collection position, the FOH indicated the perturbation to the field reduced the $\text{PPPA}_{\text{HIFU}}$ to

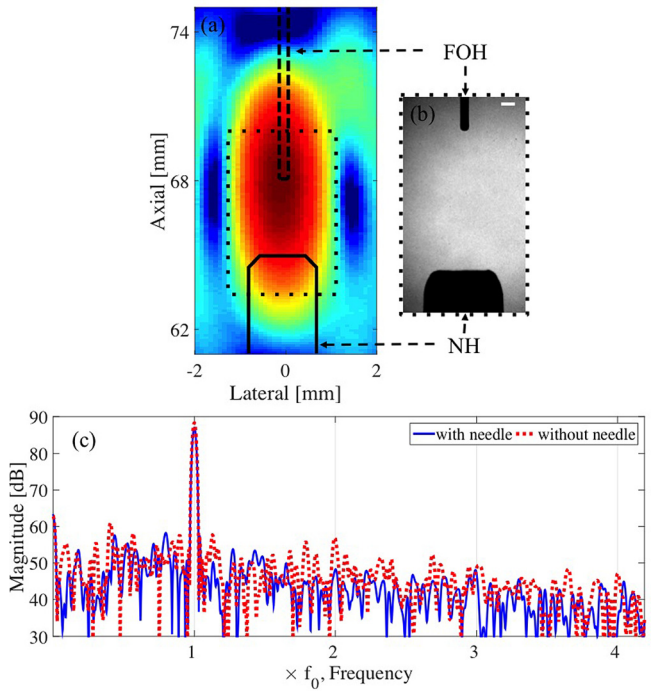

FIG. 5. (Color online) (a) Representation of the hydrophone configuration used to assess the field perturbation, introduced by the NH in the emission collection position. (b) Image depicting the NH and FOH tips during the measurements taken. Scale bar represents 250 μm. (c) Frequency spectra of HIFU field used to drive cavitation in the $f_0/3$ regime, measured by the FOH both with and without the NH in the emission collection position.

1.63 ± 0.12 and 2.42 ± 0.09 MPa, respectively, a reduction of ~15%.

A further important consideration for any acoustic field driving cavitation activity, is the harmonic content at nf_0, established due to non-linear propagation. Figure 5(c) represents the spectrum of the field, as an average of the FOH measurements taken with, and without, the NH in the emission collection position. Under free-field conditions, a $2f_0$ peak is apparent at ~30 dB less than f_0, which is also within the FOH signal-to-noise ratio (SNR). With the NH in the emission collection position, the peak appears to be somewhat suppressed, in line with a reduced $PPPA_{HIFU.}$ The NH measurements of the HIFU, with superior SNR, in the free-field conditions, confirm that low amplitude harmonics are established, at magnitudes <30 dB that of f_0.

The low *f*-number of 0.62 for the transducer used, ensures that sufficient HIFU will propagate to drive cavitation at the focus, with the NH in the emission collection position. In any case, cavitation activity responding in the desired sub-harmonic regime is confirmed by high-speed imaging.

3. Needle hydrophone deconvolution

The data recorded by the NH, including the cavitation emission signal, will be convolved with the impulse response of the hydrophone, such that the raw voltage-time signal will be distorted. Shock waves, as broadband signals, are particularly susceptible, and require deconvolution to be adequately assessed. The NH has therefore been calibrated for both magnitude and phase over a bandwidth of 125 kHz to 20 MHz in 25 kHz increments (National Physics Laboratory, Teddington, UK, 2016), such that detector deconvolution[24,38] may be implemented for PSW reconstruction. The calibration data have associated uncertainty values of 9%–12% for the magnitude and 4%–8% for the phase.

To distinguish between various data types, we introduce superscript notation, where ^{v} indicates a raw data voltage trace and ^{p} indicates the physical pressure signal. As such, the cavitation emission signal, $x^v_{cav}(t)$, detected by the NH in the voltage-time domain, is the convolution of the physical pressure signal, $x^p_{cav}(t)$, and the detector response, $h_{NH}(t)$,

$$x^v_{cav}(t) = x^p_{cav}(t) * h_{NH}(t). \tag{9}$$

Full waveform deconvolution is applied, according to

$$\tilde{X}^p_{cav}(f) = X^v_{cav}(f)/H_{NH}(f) \times H_{bpf}(f), \tag{10}$$

where $\tilde{X}^p_{cav}(f)$ is the estimated spectrum after deconvolution within the calibration bandwidth, $X^v_{cav}(f) = FT\{x^v_{cav}(t)\}$ and $H_{NH}(f) = FT\{h_{NH}(t)\}$, the complex (magnitude and phase) hydrophone sensitivity, known for 125 kHz to 20 MHz. $H_{bpf}(f)$ is a bandpass filter of the same bandwidth as the NH calibration. The estimated deconvolved pressure time waveform, within the calibration bandwidth can then be obtained as $\tilde{x}^p_{cav}(t) = FT^{-1}\{\tilde{X}^p_{cav}(f)\}$.

Another important property of any hydrophone used to detect shock waves, is the rise time, indicating how quickly the device can respond to a sudden increase in pressure. Using the OBSW generated by focusing a high energy laser-pulse into water to form a plasma, described in the Appendix, an upper bound for the rise time of the NH is estimated as 22.5 ns.

III. RESULTS

A. $f_0/2$ regime

1. High-speed imaging and needle hydrophone data

Figures 6(a)–6(c) represent high-speed imaging data captured for cavitation driven by a $PPPA_{HIFU} = 1.63 \pm 0.12$ MPa. The activity appears to consist of a single bubble, undergoing pseudo-spherical oscillation, with alternating strong collapses coincident to shock wave emission at $f_0/2$, captured Fig. 6(b) at 8.25, 14.05, 17.05 μs and arrowed, Fig. 6(c), and intervening partial deflations. It is known that for shadowgraphic imaging of acoustic transients, the focal plane for best resolution of the pressure fluctuations is slightly removed from the plane within which the emitting bubble is located.[25] For this reason, the bubble of Figs. 6(a)

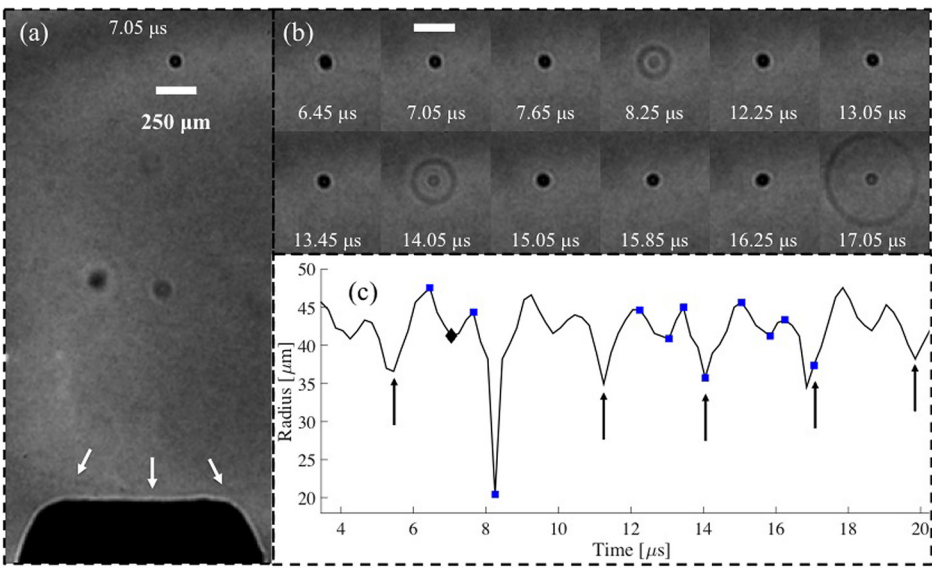

FIG. 6. (Color online) Images extracted from a high-speed sequence recorded at 5×10^6 fps, of cavitation activity in the $f_0/2$ regime. (a) The whole field of view, depicting the NH tip position relative to the activity, with a shock wave (arrowed white) incident to it. (b) Selected images representing the cavitation oscillation dynamics, including three strong collapses, and coincident shock wave emission. The entire image sequence is available, in movie format, as supplementary material (Ref. 37). (c) Radius-time curve based on a dark pixel counting algorithm, for the time interval under investigation. Diamond and squares indicate the specific images represented in (a) and (b), respectively. Scale bar represents 250 μm.

and 6(b) is slightly out of focus, and the bubble oscillation is not optimally resolved. Nonetheless, the data confirm the cavitation behavior reported previously,[13] for a HIFU-cloud system in the $f_0/2$ regime. Figure 6(c) represents the bubble radius variation with time, graphically, determined from the entire image sequence captured for this experiment.

Figure 7(a) is the raw voltage signal collected by the NH in the emission collection position. A control experiment, for which the HIFU burst was generated, but no laser-pulse incident to nucleate cavitation, is also represented. Subtraction of the control, and NH deconvolution within the calibration bandwidth via Eqs. (9) and (10) generates Fig. 7. Figures 7(b) and 7(c) show the cavitation emission signal, $\tilde{x}^p_{\text{cav}}(t)$, and the cavitation emission spectrum, $\tilde{X}^p_{\text{cav}}(f)$, respectively.

There is a propagation time from each shock wave is emitted by the cloud and imaged during by high-speed data acquisition, Fig. 6, and detection at the needle hydrophone, Fig. 7, of ~1.8–1.9 μs, depending on the precise timing of cloud collapse and shock wave emission. The propagation distance can be measured from Fig. 6(a) as ~2.7 mm; however, neither the location of the sensing element within the shaft of the NH, nor the properties of the intervening material, are known. An average propagation speed of ~1520 ms^{-1} can, however, be inferred from the high-speed imaging of PSW propagation, and a short period of supersonic propagation may be assumed.[26]

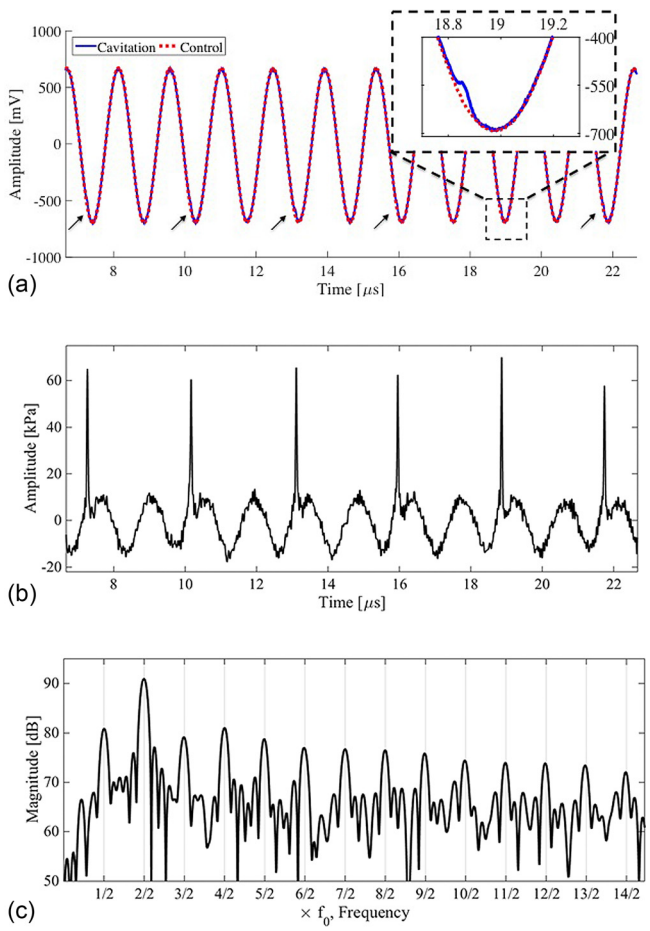

FIG. 7. (Color online) (a) Raw NH data recorded during the cavitation activity of Fig. 6 (blue solid) and control exposure for an equivalent HIFU burst (red dot), without cavitation nucleation. The inset zoom around 19.0 μs, reveals a detected shock wave in the raw data, also arrowed for the rest of the trace. (b) Control subtracted and NH-deconvolved data, revealing the signal emitted by the cavitation, $\tilde{x}^p_{\text{cav}}(t)$, captured in the high-speed imaging of Fig. 6. (c) The cavitation spectrum $\tilde{X}^p_{\text{cav}}(f)$, obtained via FT of (b).

2. Synthetic cavitation signal and spectrum

Inspection of Fig. 7(b) indicates that the estimated cavitation emission signal, $\tilde{x}^p_{\text{cav}}(t)$, is comprised of an acoustic wave (AW) component, $\tilde{x}^p_{\text{AW}}(t)$, discussed below, and $\tilde{x}^p_{\text{PSW}}(t)$, manifested as $f_0/2$ PSWs, of average period $T_{\text{PSW}} = 2.896 \pm 0.038$ μs and $\text{PPPA}_{\text{SW}} = 63.5 \pm 4.29$ kPa. We note that the PPPA_{SW} values of the individual shock waves are likely overestimated due to superpositioning over the AW component, but that the shock waves are detected close to zero pressure values within that wave.

In order to elucidate the contribution of component signals to the spectrum of the emitted signal, $\tilde{X}^p_{\text{cav}}(f)$ of Fig. 7(c), we construct a synthetic spectrum,[27,28] starting with simulated shock wave profiles. To meaningfully implement $s_{\text{sim}}(t)$ from Sec. II A 2, for direct comparison to $\tilde{x}^p_{\text{PSW}}(t)$, it is necessary to filter $s_{\text{sim}}(t)$ according to the calibration bandwidth of the needle hydrophone. This is achieved via application of $H_{\text{bpf}}(f)$, such that $S^{\text{bpf}}_{\text{sim}}(f) = S_{\text{sim}}(f) \times H_{\text{bpf}}$, which is retrieved to the time domain as $s^{\text{bpf}}_{\text{sim}}(t) = FT^{-1}\{S^{\text{bpf}}_{\text{sim}}(f)\}$.

A synthetic PSW signal, comprising six $s^{\text{bpf}}_{\text{sim}}(t)$ waveform profiles, is constructed via positioning of a $s^{\text{bpf}}_{\text{sim}}(t)$ to coincide with each of the PSWs detected experimentally, and normalized to fit the measured PPPA_{SW} of that detected shock wave. This matching is illustrated in Fig. 8(a), with the total synthetic PSW signal depicted in Fig. 8(b). In accordance with the spectral analysis model developed in Sec. II A 1, the spectrum of the synthetic PSWs, Fig. 8(c), demonstrates peaks at all the frequency values of the experimental spectrum.

We note from Fig. 8(a), that the full width at half maximum (FWHM) of $s^{\text{bpf}}_{\text{sim}}(t)$ underestimates that of $\tilde{x}^p_{\text{PSW}}(t)$, for each of the PSWs under consideration. As the spectral analysis model indicates that the PSWs make significant contributions at $nf_0/2$, including nf_0, it is reasonable to expect some underestimation across all spectral peaks, for the synthetic PSW spectrum, Fig. 8(c).

The magnitude of the peak at f_0, however, is disproportionately underestimated, as is $2f_0$ to a lesser extent. These deficits may be attributed to acoustic wave (AW) components. To estimate the AW component, $\tilde{x}^p_{\text{AW}}(t)$, we analyze the sections of experimentally detected signal between the shock waves, such as that highlighted by blue-dash [see Fig. 9(a)]. The signal section intervals are selected so that the data sampled starts 200 ns after the instant of PPPA_{SW} of preceding shock wave, and ends 400 ns before the next. This provides as long a signal as possible for analysis, whilst reducing the influence of the shock waves, and the gradual rises, to a reasonable level.

An amplitude and phase for the f_0 component from each section is determined by the FT of each signal section,

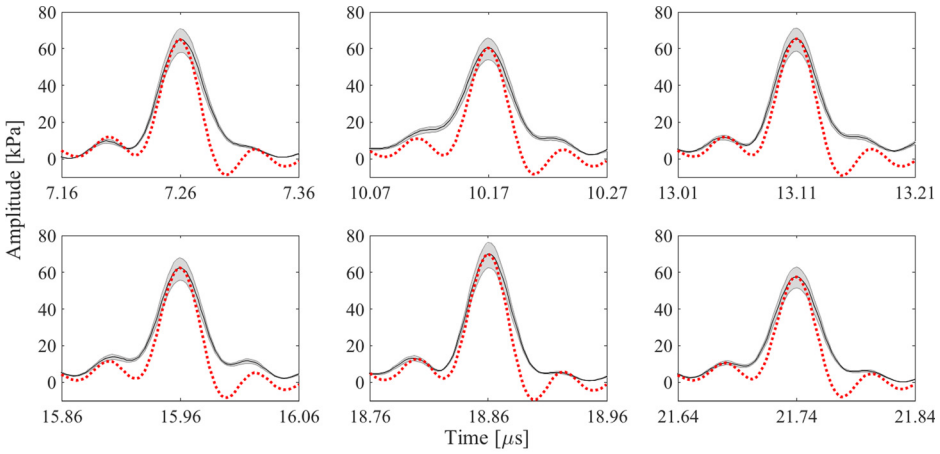

(a)

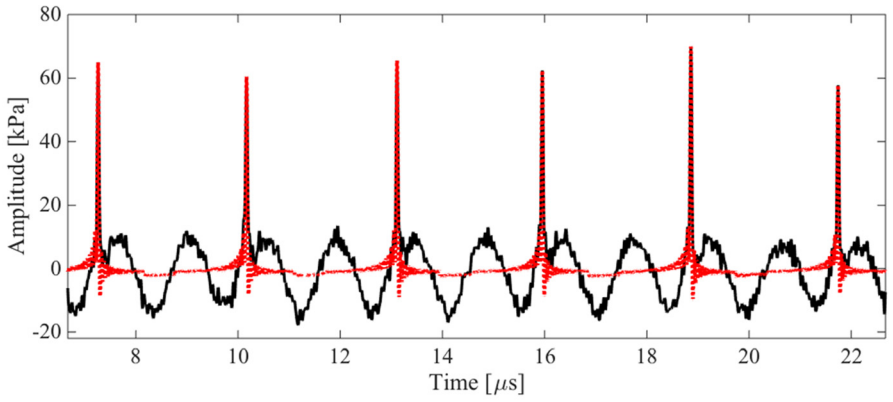

(b)

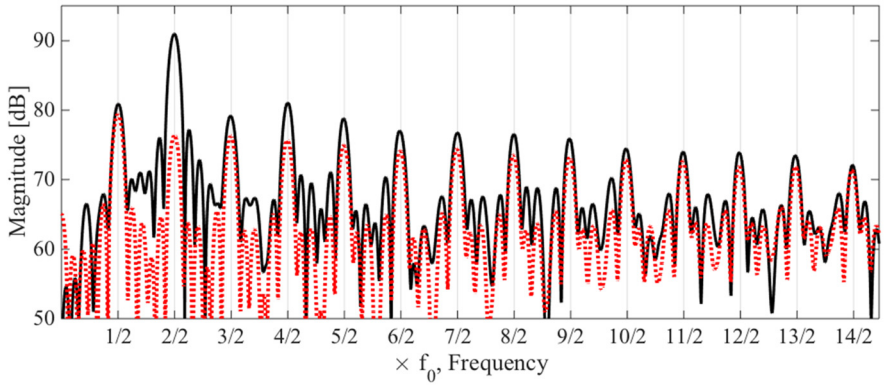

(c)

FIG. 8. (Color online) (a) The filtered simulated shock wave profiles, $s_{sim}^{bpf}(t)$, fitted to each of the shock waves detected experimentally, in the $f_0/2$ regime. The grey envelope represents the calibration uncertainty, incorporated via the deconvolution process. (b) The synthetic PSW signal (red dot), overlaid to the experimentally detected signal $\tilde{x}_{cav}^{p}(t)$ (solid black). (c) The synthetic PSW spectrum overlaid to the experimentally measured cavitation emission spectrum, $\tilde{X}_{cav}^{p}(f)$.

giving a mean value of $A_{f_0} = 11.13 \pm 0.58$ kPa and $\theta_{f_0} = 57.68° \pm 4.22°$, for the whole signal of Fig. 9(a).

As Fig. 8(c) also indicates a deficit at $2f_0$, in comparison with the experimental cavitation spectrum $\tilde{X}_{cav}^{p}(f)$, we again analyze the signal sections, such as highlighted in Fig. 9(a), for this component. The synthetic f_0 component, described previously, is subtracted from each section to minimize the side lobe of the f_0 peak, and an FT of the remaining signal taken to give amplitude and phase values of $A_{2f_0} = 0.96 \pm 0.34$ kPa and $\theta_{2f_0} = -150.35° \pm 11.52°$, respectively. Addition of these synthetic AW components to the synthetic PSW signal generates the total synthetic cavitation emission signal, Fig. 9(a), and its spectrum Fig. 9(b). The cross-correlation coefficient between the experimentally detected, and NH-deconvolved signal, and the synthetic signal is 0.97.

B. $f_0/3$ regime

Increasing the pressure amplitude of the HIFU driving is known to elevate the non-linear response of the HIFU-cloud system, such that the cloud collapse at nf_0/m for increasing m.[13] In this section, the $PPPA_{HIFU}$ is increased such that the cloud responds at $f_0/3$, and the signal analysis procedure described for the $f_0/2$ regime is repeated.

Figures 10(a)–10(c) represents high-speed imaging data captured for a laser-nucleated cavitation cloud, driven by

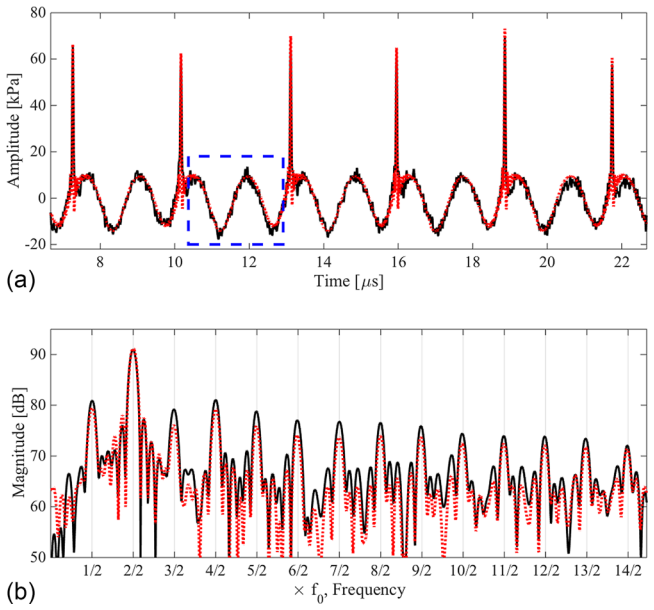

FIG. 9. (Color online) (a) The synthetic cavitation signal (red dot) composed of filtered simulated shock wave profiles, $s^{\text{bpf}}_{\text{sim}}(t)$, and synthetic AW of f_0 and $2f_0$, overlaid to the experimentally detected signal $\tilde{x}^{p}_{\text{cav}}(t)$ (solid black). (b) The synthetic cavitation spectrum, overlaid to the measured cavitation emission spectrum, $\tilde{X}^{p}_{\text{cav}}(f)$.

$\text{PPPA}_{\text{HIFU}} = 2.42 \pm 0.09$ MPa, according to the FOH, with the NH in the emission collection position.

In comparison to Figs. 6(a)–6(c) for the $f_0/2$ regime, a larger cloud consisting of a number of component bubbles has formed, consistent with higher $\text{PPPA}_{\text{HIFU}}$ causing higher levels of fragmentation. A direct consequence of a larger, non-spherical cloud, is multi-fronted shock waves emitted during the strong collapses, arrowed at 34.21 μs and 47.21 μs, Fig. 10(b). The cloud oscillation behavior of, in this case, two partial deflations between each strong collapse, is better represented by the cloud radius-time curve assessed via dark pixel counting [Fig. 10(c)], than for the $f_0/2$ imaging data [Fig. 6(c)].

Figure 11(a) are the NH-deconvolved PSWs, emitted by the strong collapses depicted in Fig. 10(c), with a 1.7–1.8 μs propagation delay time, as the cloud was located ~2.5 mm from the tip for this experiment. The first and sixth shock waves, emitted around 27.18 and 49.00 μs, are comprised of at least two separate fronts, which are resolved by the needle hydrophone. Closer inspection of the high-speed image at 34.21 μs, Fig. 10(b) indicates that this shock wave is also multi-fronted, although this is not resolved by the NH, at ~35.96 μs, Fig. 11(a). However, the underestimation of the FWHM of the NH-deconvolved shock wave, by $s^{\text{bpf}}_{\text{sim}}(t)$, is noticeably larger for this shock wave than for the others of Fig. 11(a). This is compatible with the NH registering more than one shock wave profile, but failing to resolve the component shock wave peaks.

The average shock wave period, $T_{\text{PSW}} = 4.36 \pm 0.08$ μs, with mean detection times used for multi-front emission. For single-fronted shock waves according to the NH data the average $\text{PPPA}_{\text{SW}} = 108.09 \pm 11.86$ kPa. The larger PPPA_{SW} of the shock waves emitted in the $f_0/3$ regime, compared to those measured at $f_0/2$, can be attributed to the collapse of a larger cloud, under higher amplitude $\text{PPPA}_{\text{HIFU}}$.

Figure 11(a) depicts the fitting of the filtered simulated shock waves, $s^{\text{bpf}}_{\text{sim}}(t)$, to those detected experimentally, which are compiled to produce the synthetic PSW signal. The AW components at f_0 and $2f_0$ are estimated consistent with the approach adopted previously for the $f_0/2$ regime, as $A_{f_0} = 35.49 \pm 2.20$ kPa, $\theta_{f_0} = 111.78 \pm 1.16°$, $A_{2f_0} = 2.47 \pm 0.19$ kPa and $\theta_{2f_0} = 27.30 \pm 10.87°$. The total synthetic signal and its spectrum are presented in Figs. 11(b) and 11(c), with a cross-correlation coefficient of 0.97 to the experimentally detected, and NH-deconvolved signal.

IV. DISCUSSION

The experiments described allow interrogation of cavitation activity at unprecedented detail, both optically and acoustically. The results confirm a previously unidentified and significant contribution of periodic shock waves from acoustically driven cavitation, to the spectrum of the emitted signal, according to the spectral analysis model presented in Sec. II A 1. We note that the experimental results presented

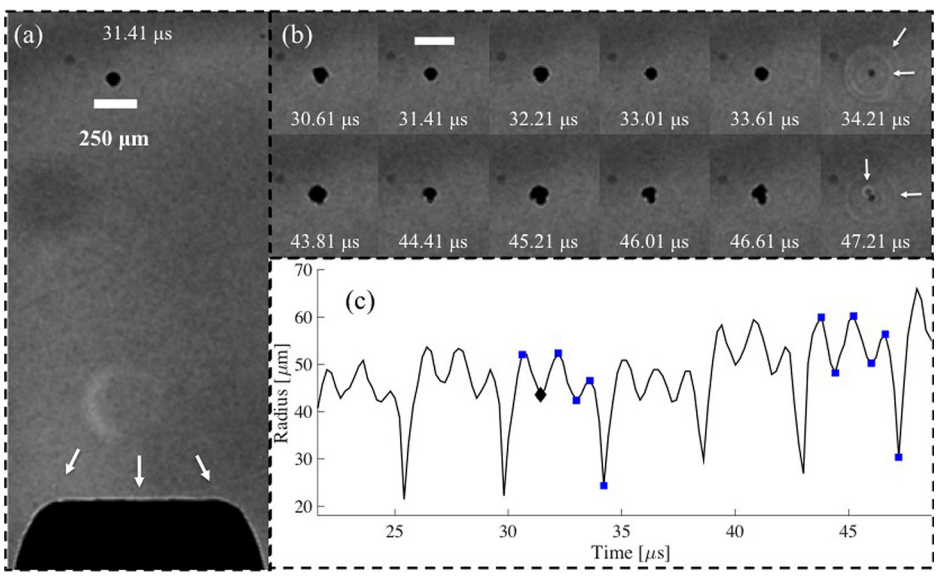

FIG. 10. (Color online) Images extracted from a high-speed sequence recorded at 5×10^6 fps, of cavitation activity in the $f_0/3$ regime. (a) The whole field of view, and (b) selected images representing the cavitation oscillation dynamics, including the third and sixth strong collapses, as presented in (c) radius-time curve based on a dark pixel count algorithm, for the time interval under investigation. Diamond and squares indicate the specific images represented in (a) and (b), respectively. The entire image sequence is available, in movie format, as supplementary material (Ref. 37). Scale bar represents 250 μm.

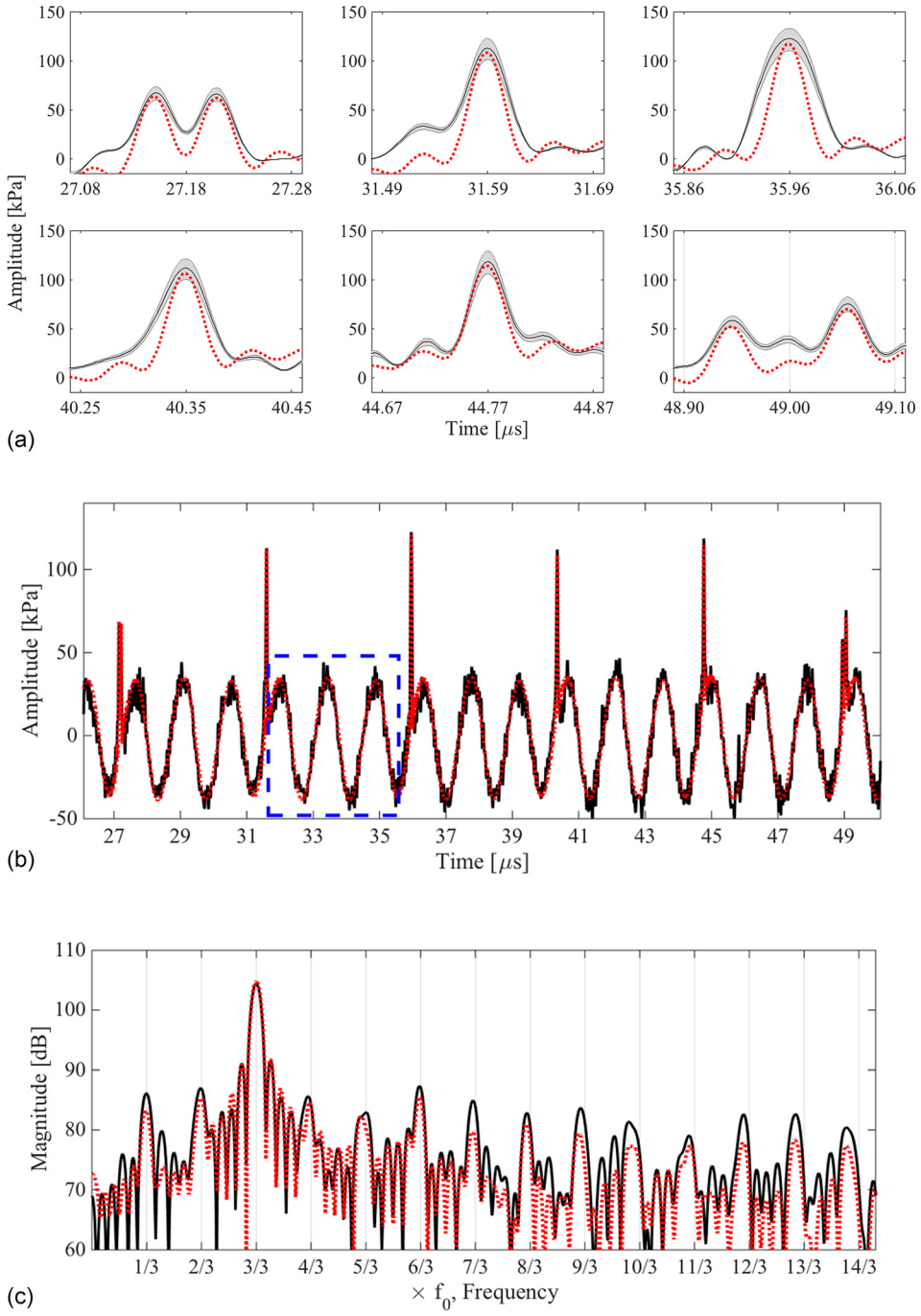

FIG. 11. (Color online) (a) The filtered simulated shock wave profiles, $s_{\mathrm{sim}}^{\mathrm{bpf}}(t)$, fitted to each of the shock waves detected experimentally, in the $f_0/3$ regime. The grey envelope represents the calibration uncertainty, incorporated via the deconvolution process. (b) The synthetic cavitation emission signal (dotted red), with acoustic emission components $\tilde{x}_{\mathrm{AW}}^{p}(t)$ added, overlaid to the experimentally measured cavitation emission signal (solid black). (c) The synthetic PSW spectrum, overlaid to the experimentally measured cavitation emission spectrum, $\tilde{X}_{\mathrm{cav}}^{p}(f)$.

above have been selected from longer data sets, as ideal cases in terms of shock wave periodicity, to demonstrate this contribution.

To compare the amplitudes of the emitted signal components $x_{\mathrm{PSW}}(t)$ and $x_{\mathrm{AW}}(t)$, the root mean square (RMS) amplitudes of the synthetic $f_0/2$ signal is calculated, Fig. 9(a), as 6.58 and 7.90 kPa, respectively. Moreover, the experimental cavitation spectra can be well approximated as a series of bubble-collapse shock waves and an acoustic f_0 component. Under this approximation, the non-linearity of the cavitation emission signal is concentrated within the shock wave content, or in terms of bubble oscillation, the collapse phases.

The key aspect behind the spectral analysis of PSWs is the periodicity of the shock waves. A single shock wave, or many aperiodic shock waves may be expected to contribute via raising the noise floor of the spectrum. In contrast, *periodic* shock waves, emitted sub-harmonically at f_0/m, must provide spectral peaks at nf_0/m, for all values of n and m. Moreover, sub-harmonic features should not occur in isolation from their respective over-harmonics. From the broadband nature of the shock waves, detection of cavitation activity can be undertaken at any mf_0/n peak. Nevertheless, experimental constraints such as absorption of higher frequency content and detector characteristic should be taken into account when selecting a monitoring protocol.

We further note that the spectral model suggests that any periodic or non-periodic non-linear emission from cavitation, generally, will result in spectral features manifested as harmonic peaks or elevated broadband noise, respectively.

Recent theoretical endeavors, based on single bubble oscillations suggest that the physical insight to the sub-harmonic cavitation response, specifically the bifurcations at higher driving amplitudes, may be found in non-linear oscillator theory.[29,30]

For the purposes of constructing synthetic spectra, we have considered the cavitation emissions as separate components. It should be emphasized, however, that the cavitation signal is continuously emitted according to the source bubble dynamics, and should not generally be considered as individually emitted components. This point is particularly pertinent when considering the simulated BCSW profile of Fig. 3, and that detected from a laser-induced bubble collapse in the Appendix [Fig. 12(c)(ii)], particularly in contrast to the OBSW of Fig. 12(c)(i). BCSW profiles exhibit a characteristic gradual rise to $PPPA_{SW}$, appreciable several tenths of a microsecond before the time of $PPPA_{SW}$, and distinct to the sharp rise typical of other shock wave profiles, including the OBSW. This gradual rise is generated by the bubble emitting as it deflates into the collapse, with the spike of the shock wave generated at the moment of minimum radius. For PSWs emitted from driven clouds, the gradual rise will be irrevocably imposed over the acoustic emissions, or rather is an integral to them. The influence of the gradual rise is also apparent in Fig. 9(a), where the alternating troughs of the acoustic signal component, preceding the shock wave detections, are elevated relative to the other troughs, by 2.36 ± 0.71 kPa, for this data.

For both the $f_0/2$ and $f_0/3$ regimes, the synthetic PSW signal underestimated the magnitude of all spectral features within the respective cavitation spectra, detected experimentally. Inspection of the simulated shock waves, normalized to the pressure amplitude of the experimentally detected NH-deconvolved shock waves, indicates that the FWHMs are also consistently underestimated, in the synthetic signal Figs. 8(a) and 11(a). We speculate that one source of this underestimation is a spreading effect, across the tip of the needle hydrophone, during shock wave detection. This effect can be appreciated from Figs. 6(a) and 10(a), where direct observation of the shock wave confirms that the shock front is initially incident to the sensing surface at the point directly below the cavitation cloud position. As the shock wave spreads across the tip, the detected FWHM will become extended in duration. Considering the geometry of the experimental configuration, we estimate the effect of shock wave spreading to be several tens of ns of widening for the FWHM of the detected shock wave profile. A detector with a smaller active area, or placed further from the cavitation activity would reduce the radius of curvature of the shock wave on detection, leading to better matching between the experimental and simulated shock wave profiles.

Recently, limitations to the Gilmore equation as applied to strong inertial collapses for which R_0/R_{max} is less than $\sim$0.1, have been reported.[31,32] Refined computations, accounting for non-linear liquid compressibility effects and non-uniform internal pressure, would yield a more accurate bubble collapse curve than that used here, in Fig. 3, where $R_0/R_{max} \sim 0.09$. Moreover, there are more sophisticated bubble collapse shock wave propagation models[33] than the linear approximation we have used, Eq. (8). Higher precision simulations would be expected to deliver a better representation of the physical shock wave. However, the experimentally retrieved shock waves, which are deconvolved over a limited calibration bandwidth for the hydrophone used, appear to be sufficiently represented for the purpose of synthetic spectrum construction.

The synthetic f_0, as the dominant component required to fit the synthetic spectra to those measured experimentally, may be attributed to scattering of the primary field, or linear bubble oscillation-generated emission. The underestimation of the $2f_0$ peak of the experimental spectra, by the synthetic PSW signal, could indicate some non-linearity of the bubble oscillations between collapses. However, the gradual rise of the PSWs will not have been fully removed by the selecting of the signal sections from 200 ns after, to 400 ns before, the $PPPA_{SW}$. The $2f_0$ component could originate from either of these sources, or some combination of both.

In terms of the cavitation activity itself, these observations align with speculation from recent literature[34] that the conventional, binary classification of cavitation as stable or unstable/inertial is inadequate. The cavitation from the $f_0/2$ regime of Fig. 6 is, in every sense other than the collapse-mediated shock wave generation, activity that would be described as stable. The oscillations are periodic and of regular amplitude in terms of the bubble radius, and there is no indication of fragmentation events during the collapses. Nonetheless, shock waves, which are synonymous with inertial cavitation, form a significant component of the emitted signal. The $f_0/3$ activity at higher HIFU driving of Fig. 10, may be interpreted as exhibiting stronger inertial characteristics, particularly the fragmentation that has led to the formation of a bubble cloud. The cloud is of irregular morphology for each oscillation, with bubbles or small sub-clusters of bubbles within the cloud, collapsing individually to generate multi-fronted shock waves. The effect of multi-fronted shock waves on the cavitation spectrum is the formation of broadened and misshaped peaks, which are reproduced by the spectral analysis model when simulated shock waves of variable $PPPA_{SW}$ and emission times are used. These observations indicate that a spectrum of cavitation activity exists between the extremes of the classic linear-stable and chaotic-inertial categories.[35] Periodic shock wave emission and generation of the sub-harmonic signal at $f_0/2$ could mark the first departure from classically stable cavitation, into stable-inertial, with increasing of the driving amplitude.

V. CONCLUSION

We present a simple spectral analysis model demonstrating a significant contribution to the cavitation spectrum from periodic shock waves, at nf_0/m peaks for all values of n and m, with supporting experimental data for $m = 2$ and 3. We conclude that simultaneous detection of the sub-harmonic signal at f_0/m, with higher-order sub-harmonics at nf_0/m, is suggestive of a cavitating system that is generating periodic shock waves. Moreover, the binary classification of cavitation into stable or inertial categories is inadequate, and that an intermediate "stable-inertial" category is required.

ACKNOWLEDGMENTS

The research leading to these results has received funding from the European Research Council under the European Union's Seventh Framework Programme (FP/2007–2013)/ERC Grant No. 336189 (TheraCav). The authors acknowledge Keith Johnston, Graeme Casey, and Miriam Jiménez García for technical assistance, and Dr. Helen Mulvana for use of the fiber-optic hydrophone.

APPENDIX: ASSESSMENT OF HYDROPHONE RISE TIME

An important characteristic of any detector used to measure a shock wave is the rise time (RT), which may be defined as the time taken to rise from 10% of the maximum signal amplitude, to 90%, in response to a step function with zero-RT. If the RT of a particular detector is not shorter than the physical RT of the shock wave it is measuring, then a good estimate of the $PPPA_{SW}$ may not be taken. It is difficult to implement a step function experimentally, however, a good approximation that can be realized with the experimental arrangement described, is the shock wave generated when a laser pulse of energy above the breakdown threshold, is focused into the water. This is a well-documented approach to studying large ($R_{max} \sim 100$'s μm) plasma-mediated, vapor bubbles dynamics, often referred to as a laser-induced bubble (LIB) [Fig. 12(a)], for applications such as ophthalmology.[36] An LIB initially undergoes a rapid expansion phase in response to the energy deposition, which the inertia of the host medium decelerates, eventually causing the bubble to contract and collapse. Acoustic detection of the LIB process is characterized by the emission of two shock waves. The first is generated by the optical breakdown (OBSW) on absorption of the laser pulse,[15] with the second emitted during the bubble collapse (BCSW) after a duration equal to the oscillation period of the LIB [Fig. 12(b)].

Through calculation and experiment with a pulsed laser similar to the one used in our experiments, Vogel *et al.*[15] indicate an OBSW with a RT of ~6 ns and an initial $PPPA_{SW}$ in the order of a GPa, may be expected.

Accordingly, we employ a laser pulse of energy 4.0 ± 0.2 mJ (instrument error, according to manufacturer) to generate an OBSW, to assess the RT of the needle hydrophone, and therefore its suitability for measuring the PSWs. To avoid damage to the hydrophone through exposure to such a high amplitude, the tip is located ~50 mm from the LIB location, during the acquisition of the data presented, Fig. 12(b). In this position, planar incidence to the 1 mm tip may also be assumed.

Figure 12(c) depicts the OBSW and BCSW profiles. Clearly, the rise from ambient pressure for the OBSW is much sharper than that of the BCSW, as an approximation to a step function, with an RT $\approx$ 22.5 ns measured from the detected profile between the red arrows. As the physical OBSW itself has a non-zero RT, 22.5 ns can thus be taken as an upper bound for the actual RT of the NH. The RT of the measured BCSW profile, Fig. 12(b) is ~73 ns, due to the gradual rise integral to the shock wave generated by a bubble collapse profile. The $PPPA_{SW}$ of the BCSW is therefore reasonably estimated, as opposed to that of the OBSW. By

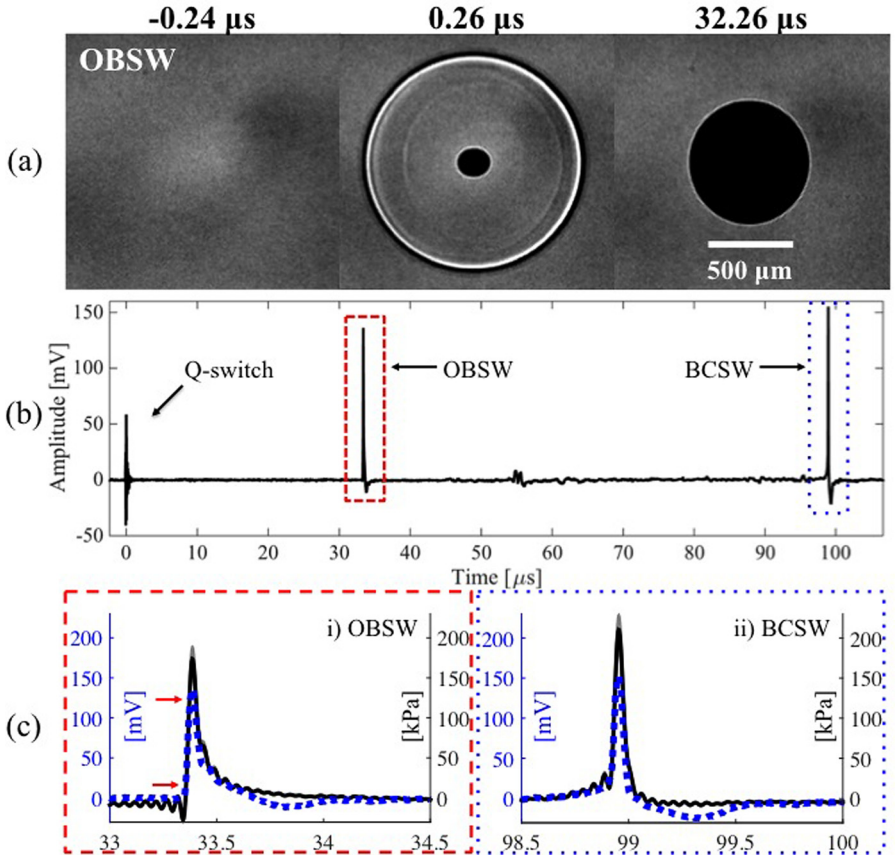

FIG. 12. (Color online) Approximation of the needle hydrophone RT using an OBSW: (a) Representative frames from a high-speed image sequence, taken at 2×10^6 fps, showing the formation of an LIB, with the laser Q-switch taken as $t = 0$ μs, and propagation of the OBSW that is generated, at 0.26 μs. The LIB continues to expand up to its maximum radius, captured at 32.26 μs, followed by collapse (data not shown). (b) The hydrophone trace detected, with the tip located ~50 mm from the LIB location. (c) Higher temporal resolution of the OBSW and BCSW profiles (blue dash). Deconvolved shock waves are also presented (solid black). Arrows indicate 10% and 90% of peak voltage amplitude.

extension, the $PPPA_{SW}$'s of the PSWs emitted by the cavitation activity in the main manuscript are reasonably estimated, within the limit of the calibration bandwidth of the NH.

[1]T. G. Leighton, *The Acoustic Bubble* (Academic, London, 1994), Chaps. 4 and 5, pp. 413–524.
[2]V. F. Humphrey, "Nonlinear propagation in ultrasonic fields: Measurements, modelling and harmonic imaging," Ultrasonics **38**, 267–272 (2000).
[3]C. M. Schoellhammer, A. Schroeder, R. Maa, G. Y. Lauwers, A. Swiston, M. Zervas, R. Barman, A. M. DiCiccio, W. R. Brugge, D. G. Anderson, D. Blankschtein, R. Langer, and G. Traverso, "Ultrasound-mediated gastrointestinal drug delivery," Sci. Transl. Med. **7**, 310ra160–310ra168 (2015).
[4]M. A. O'Reilly and K. Hynynen, "Blood-brain barrier: Real-time feedback-controlled focused ultrasound disruption by using an acoustic emission-based controller," Radiology **263**, 96–106 (2012).
[5]J. McLaughlan, I. Rivens, T. Leighton, and G. ter Haar, "A study of bubble activity generated in *ex vivo* tissue by high intensity focused ultrasound," Ultrasound Med. Biol. **36**, 1327–1344 (2010).
[6]R. Esche, "Investigation of acoustic cavitation in liquids," Acustica **2**, AB208–218 (1952).
[7]J. Sijl, B. Dollet, M. Overvelde, V. Garbin, T. Rozendal, N. de Jong, D. Lohse, and M. Versluis, "Subharmonic behavior of phospholipid-coated ultrasound contrast agent microbubbles," J. Acoust. Soc. Am. **128**, 3239–3252 (2010).
[8]J. T. Tervo, R. Mettin, and W. Lauterborn, "Bubble cluster dynamics in acoustic cavitation," Acta Acoust. **92**, 178–180 (2006).
[9]D. M. Hallow, A. D. Mahajan, T. E. Mccutchen, and M. R. Prausnitz, "Measurement and correlation of acoustic cavitation with cellular bioeffects," Ultrasound Med. Biol. **32**, 1111–1122 (2006).
[10]P. R. Birkin, D. G. Offin, C. J. B. Vian, and T. G. Leighton, "Multiple observation of cavitation cluster dynamics close to an ultrasonic horn tip," J. Acoust. Soc. Am. **130**, 3379–3388 (2011).
[11]W. Lauterborn and A. Koch, "Holographic observation of period doubled and chaotic bubble oscillations in acoustic cavitation," Phys. Rev. A **35**, 1974–1976 (1987).
[12]W. Lauterborn, T. Kurz, R. Mettin, and C. D. Ohl, "Experimental and theoretical bubble dynamics," Adv. Chem. Phys. **110**, 295–380 (1999).
[13]K. Johnston, C. Tapia-Siles, B. Gerold, M. Postema, S. Cochran, A. Cuschieri, and Paul Prentice, "Periodic shock-emission from acoustically driven cavitation clouds: A source of the subharmonic signal," Ultrasonics **54**, 2151–2158 (2014).
[14]Y. Zhou, "Reduction of bubble cavitation by modifying the diffraction wave from a lithotripter aperture," J. Endourol. **26**, 1075–1084 (2012).
[15]A. Vogel, S. Busch, and U. Parlitz, "Shock wave emission and cavitation bubble generation by picosecond and nanosecond optical breakdown in water," J. Acoust. Soc. Am. **100**, 148–165 (1996).
[16]A. Vogel and W. Lauterborn, "Acoustic transient generation by laser-produced cavitation bubbles near solid boundaries," J. Acoust. Soc. Am. **84**, 719–731 (1988).
[17]C. C. Church, "A theoretical study of cavitation generated by an extracorporeal shock wave lithotripter," J. Acoust. Soc. Am. **86**, 215–227 (1989).
[18]A. Prosperetti and A. Lezzi, "Bubble dynamics in a compressible liquid. Part 1. First-order theory," J. Fluid Mech. **168**, 457–478 (1986).
[19]W. Kreider, L. A. Crum, M. R. Bailey, and O. A. Sapozhnikov, "A reduced-order, single-bubble cavitation model with applications to therapeutic ultrasound," J. Acoust. Soc. Am. **130**, 3511–3530 (2011).
[20]J. R. Macdonald, "Some simple isothermal equations of state," Rev. Mod. Phys. **38**, 669–679 (1966).
[21]M. Minnaert, "On the musical air-bubbles and the sound of running water," Philos. Mag. **16**, 235–248 (1933).
[22]C. E. Brennen, "Cavitation in medicine," Interface Focus **5**, 2010022 (2015).
[23]B. Gerold, S. Kotopoulis, C. McDougall, D. McGloin, M. Postema, and P. Prentice, "Laser-nucleated acoustic cavitation in focused ultrasound," Rev. Sci. Inst. **82**, 044902 (2011).
[24]A. Hurrell, "Voltage to pressure conversion: Are you getting 'phased' by the problem?," J. Phys.: Conf. Series, Adv. Metrol. Ultrasound Med. **1**, 57–62 (2004).
[25]N. Kudo, "A simple technique for visualizing ultrasound fields without Schlieren optics," Ultrasound Med. Biol. **41**, 2071–2081 (2015).
[26]E. A. Brujan, T. Ikeda, and Y. Matsumoto, "Shock wave emission from a cloud of bubbles," Soft Matter **8**, 5777–5783 (2012).
[27]E. Cramer and W. Lauterborn, "Acoustic cavitation noise spectra," Appl. Sci. Res. **38**, 209–214 (1982).
[28]J. Eisener and R. Mettin, "Synthetic acoustic spectra of ultrasonic cavitation emissions," in *Fortschritte der Akustik - DAGA 2012 Darmstadt, Deutsche Gesellschaft für Akustik e.V.*, edited by H. Hanselka (DEGA, Berlin, 2012), pp. 435–436.
[29]C. Scheffczyk, U. Parlitz, T. Kurz, W. Knop, and W. Lauterborn, "Comparison of bifurcation structures of driven dissipative nonlinear oscillators," Phys. Rev. A **43**, 6495–6502 (1991).
[30]V. Englisch, U. Parlitz, and W. Lauterborn, "Comparison of winding-number sequences for symmetric and asymmetric oscillatory systems," Phys. Rev. E **92**, 022907 (2015).
[31]D. Fuster, C. Dopazo, and G. Hauke, "Liquid compressibility effects during the collapse of a single cavitating bubble," J. Acoust. Soc. Am. **129**, 122–131 (2011).
[32]M. Koch, C. Lechner, F. Reutera, K. Köhlera, R. Mettina, and W. Lauterborna, "Numerical modeling of laser generated cavitation bubbles with the finite volume and volume of fluid method, using OpenFOAM," Comput. Fluids. **126**, 71–90 (2016).
[33]E. Cramer and W. Lauterborn, "On the dynamics and acoustic emission of spherical cavitation bubbles in a sound field," Acustica **49**, 226–238 (1981).
[34]C. C. Church and E. L. Carstensen, "'Stable' inertial cavitation," Ultrasound Med. Biol. **27**, 1435–1437 (2001).
[35]W. Lauterborn and E. Cramer, "Sub-harmonic route to chaos observed in acoustics," Phys. Rev. Lett. **47**, 1445–1448 (1981).
[36]E.-A. Brujan and A. Vogel, "Stress wave emission and cavitation bubble dynamics by nanosecond optical breakdown in a tissue phantom," J. Fluid Mech. **558**, 281–308 (2006).
[37]See supplementary material at http://dx.doi.org/10.1121/1.4964633 for the image sequence of Figs. 6 and 10.
[38]K. Johansen, J. H. Song, K. Johnston, and P. Prentice, "Deconvolution of acoustically detected bubble-collapse shock waves," Ultrasonics **73**, 144–153.